Dalton Transactions

ROYAL SOCIETY OF CHEMISTRY

PAPER

View Article Online
View Journal | View Issue

Cite this: *Dalton Trans.*, 2025, **54**, 12849

Template-driven synthesis of tin selenide nanosheets and their composites for supercapacitor applications

Nisha Kushwah,[a] Divya Nechiyil,[b] Jyoti Prakash,[c,d] Suresh M. Chopade,[a] Sushil Swaroop Pathak,[e] Amey Wadawale,[a] Sanjay Kumar[f] and Gotluru Kedarnath *[a,d]

Received 28th May 2025,
Accepted 21st July 2025

DOI: 10.1039/d5dt01255d

rsc.li/dalton

Bulk SnSe and $SnSe_2$, with direct-band gaps of 1.3 eV and 1.84 eV, are promising materials for optoelectronics, lithium-ion batteries, thermoelectrics, and supercapacitors, due to their excellent electrochemical performance for energy storage. In this context, a new molecular precursor, $[Me_2Sn(SeC_4H_3N_2)_2]$, has been derived from bis(2-pyrazinyl)diselenide {(2-pyzSe)$_2$} and structurally characterised by single crystal X-ray diffraction (sc-XRD) that serves as a building block for the fabrication of tin selenide (SnSe) nanosheets and tin selenide/g-C_3N_4 composites. The electrochemical performance of the synthesised nanosheets and composites was evaluated for their potential use in supercapacitor applications. The band gaps of rectangular SnSe (1.85 eV) and hexagonal $SnSe_2$ (2.21 eV) nanosheets, and tin selenide/g-C_3N_4 composites (1.89 and 1.91 eV) exhibited a blue shift compared to those of bulk SnSe (E_g = 1.3 eV) and $SnSe_2$ (E_g = 1.84 eV). The tin selenide/g-C_3N_4 composite utilised in supercapacitor applications exhibited a specific capacitance of 140 F g^{-1} at a current density of 1 A g^{-1}. Remarkably, it retained 85% of this specific capacitance after 5000 cycles, demonstrating outstanding cycling durability.

Introduction

The increasing global demand for energy and environmental problems, accompanied by dwindling fossil fuel reserves, are compelling us to look at clean and sustainable renewable energy sources. To address these issues, advances in effective energy conversion and storage devices, *viz.* solar cells,[1–4] electrochemical water splitting cells,[5–8] batteries[9] and supercapacitors,[10] will be essential. Among these, supercapacitors (SCs) are remarkable electrochemical energy storage devices, which present higher power densities, better safety compliance and more prompt storage and release of charge compared to batteries. Furthermore, the SCs can operate in pollution-free and rapidly changing temperature conditions, leading to extended and enduring charge/discharge cycles. In this direction, 2D layered metal chalcogenide nanostructure-based energy conversion and storage devices can further lead to path-breaking technologies. Within the class of 2D layered metal chalcogenides, tin selenide has been verified as a suitable material for its applicability in the fields of thermoelectrics,[1] photodetectors,[2] solar cells,[3] gas sensing,[4] topological insulators,[5] anode materials for batteries,[6,9] supercapacitors[10] and other related applications. Nevertheless, the category of application is strongly dependent on size, shape, composition, phase-driven properties, *etc.* Typically, tin selenide exists in two forms: SnSe and $SnSe_2$. SnSe inherently grows in an orthorhombic crystal system with bulk direct- and indirect-energy gaps of 1.3 and 0.9 eV, respectively. In contrast, $SnSe_2$, an innate n-type semiconductor, features a CdI_2-type crystal lattice and has bulk direct- and indirect-energy gaps of 1.84 and 1.07 eV, respectively.[9] The first form of tin selenide exhibits optical and structural anisotropy, making it suitable for photovoltaic[3] and thermoelectric applications,[10,11] while $SnSe_2$ shows promise in superconductivity,[12] alkali metal ion battery anodes,[13] photocatalysis,[14] and as an absorber for pulsed lasers.[15]

Additionally, the focus has also been on SnSe for supercapacitor (SC) applications. However, glitches associated with the composition or phase of tin selenides are often found during their synthesis. Accordingly, quite a few methods, including solution-phase synthesis or solvent-less approaches have

[a]*Chemistry Division, Bhabha Atomic Research Centre, Trombay, Mumbai-400085, India. E-mail: kedar@barc.gov.in*
[b]*Manipal Institute of Applied Physics, Manipal Academy of Higher Education, Manipal, Karnataka-576104, India*
[c]*Materials Group, Bhabha Atomic Research Centre, Mumbai-400085, India*
[d]*Homi Bhabha National Institute, Anushaktinagar, Mumbai-400094, India*
[e]*Laboratoire de chimie de la matière condensée de Paris, Sorbonne Universite, Paris 75005, France*
[f]*Materials Science Division, Bhabha Atomic Research Centre, Mumbai-400085, India*

emerged over a period for the synthesis of nano-tin selenides by choosing either dual-source[16–19] or single-source molecular precursor (SSMP)[20–32] methods. In the case of dual-source methods, tin sources like Sn, $SnCl_2$,[19] $SnCl_4$, tin-oleate complex, $Sn_6O_4(OH)_4$, $Sn[N(SiMe_3)_2]_2$, *etc.* and selenium sources such as Se,[16] SeO_2,[18] and Se ligand/compound[17] have been employed for the synthesis of tin selenide nanostructures with suitable selection of reaction conditions. When adopting the SSMP method, the complexes $(Bz_3Sn)_2Se$ (Bz = benzyl),[20] $[Sn(SeC_5H_4N)_2]_2$,[21] $[\{Me_2NC(NCy)_2\}_2Sn{=}Se]$,[22] $[\{(Me_3Si)_2N\}_2Sn(SePh)_2]$,[23] and $[\{Sn[N(Me_3Si)_2]_2(\mu\text{-}Se)\}_2]$[23] have been utilised for the synthesis of SnSe nanomaterials, whereas $(Ph_2SnSe)_3$[24] yielded Sn-contaminated SnSe. While our group also has effectively employed quite a few dialkyl-tin complexes consisting of heterocyclic-based internally functionalised hemilabile ligands as molecular templates for the synthesis of either SnSe or $SnSe_2$ nanostructures or thin films, by varying the alkyl groups either on tin or the ligand itself.[25–28] Recently, Mathur *et al.* demonstrated the controlled decomposition of $[Sn^{IV}(SeC_2H_4N(Me)C_2H_4Se)_2]$ and $[Sn^{IV}Cl_2(SeC_2H_4N(Me)C_2H_4Se)]$ into SnSe and $SnSe_2$ phases.[17] Moreover, $[Sn(Ph_2PSe_2)_2]$[29] and $[Bu_2Sn(PhCOSe)_2]$[30] were employed for the deposition of SnSe thin films, while $[SnCl_4(^nBu_2Se)_2]$[31] and $[SnCl_4\{^nBuSe(CH_2)_2Se^nBu\}]$[32] were employed for the growth of $SnSe_2$ thin films.

Despite these achievements for the synthesis of tin selenide nanostructures, very few synthetic protocols for the synthesis of SnSe have been presented in the literature for supercapacitor applications.[19,33] For instance, Zhang *et al.*[34] have reported SnSe disc-shaped nanosheets which exhibit a specific capacitance of 210 F g^{-1} at 1 A g^{-1}, while $SnSe_2$ nano-discs showcase 144 F g^{-1} at 1 A g^{-1} with 99% retention of capacitance after 1000 cycles. Ni *et al.* reported a specific capacitance of 214.3 F g^{-1} for microwave-synthesised SnSe.[16] Nevertheless, molecular template-based controlled synthesis of 2D SnSe nanosheets and their g-C_3N_4 composites for supercapacitor applications is rare to nonexistent, even though a number of merits have been listed for SSMPs.[35,36] For instance, SSMPs in general comprise pre-existing M–E (M = metal and E = chalcogen) linkages, allowing molecular-level mixing, resulting in greater regulation of composition and defects. The judicious selection of ligands for SSMP synthesis is useful for appreciating the cleaner decomposition of SSMP at relatively low temperatures, ensuring high-quality target materials. Further, the versatility of SSMP as a source for both nanomaterial synthesis and film deposition makes it handy for device applications.[35,36] Therefore, the synthesis of SnSe nanosheets for supercapacitor applications has been envisaged and implemented through the SSMP route.

With this perspective, a new and monomeric pyrizinylselenolate of Sn(IV), $[Me_2Sn(SeC_4H_3N_2)_2]$ (**1**), has been synthesised and unequivocally characterised using sc-XRD. Additionally, a modest and scalable synthesis of high-quality SnSe nanosheets and their g-C_3N_4 composites has been investigated for supercapacitor applications, utilising the aforementioned complex for the first time. Furthermore, a g-C_3N_4-induced phase transition from SnSe to $SnSe_2$ has also been observed during the preparation of composites. A supercapacitor made up of a tin selenide-g-C_3N_4 composite exhibits a specific capacitance of 140 F g^{-1} at 1 A g^{-1} with 85% retention of this specific capacitance up to 5000 cycles. This indicates long cycle durability with reasonable specific capacitance for the tin selenide system.

Experimental section

Materials

Prior to use, all reagents were dried and purified using standard methods. Me_2SnCl_2, $NaBH_4$, oleylamine (OAm), KOH and analytical grade solvents were purchased from commercial sources. The diselenide, $\{2\text{-}SeC_4H_3N_2\}_2$ (^{1}H NMR ($CDCl_3$) δ: 2.37 (s, Me); 6.71 (s, CH-5). $^{13}C\{^1H\}$ NMR($CDCl_3$) δ: 23.7 (Me); 117.2 (CH-5); 165.7 (C-2); 167.5 (C-4,6). $^{77}Se\{^1H\}$ NMR ($CDCl_3$) δ: 486 ppm) was prepared according to a previously reported method in the literature.[37]

The CNT films were synthesized using the floating-catalyst chemical vapor deposition (FC-CVD) method.[38,39] Briefly, a catalyst solution comprising thiophene, ferrocene, and ethanol in a weight ratio of 0.3 : 2 : 32 was preheated to 150 °C and introduced into the reactor at a flow rate of 0.2 mL min^{-1}. Argon and hydrogen gases were used as carriers at a total flow rate of 1 L min^{-1}. CNT soot was formed inside the reactor at 1250 °C, and the resulting CNT network was continuously collected in a glove box on a rotating steel rod, yielding a free-standing CNT film. The CNT aerogel films were immersed in a concentrated acid mixture of H_2SO_4 and HNO_3 (3 : 1 v/v) to improve surface wettability, thereby facilitating better electrolyte penetration and enhancing electrochemical performance. The resulting CNT substrate is highly conductive (~5000 S cm^{-1}), with a thickness of ~100 μm, and serves as a current collector for the electrode material.

Physical measurements

All reactions were conducted under an anhydrous and inert atmosphere. A Thermo Fischer Flash EA1112 CHNS elemental analyser was employed for elemental analyses. Electronic spectra were acquired on a UV–vis Jasco V-630 spectrophotometer. The multinuclear NMR spectra (^{1}H, $^{13}C\{^1H\}$ and $^{125}Se\{^1H\}$) were obtained on a Bruker Avance-II spectrometer operating at 300, 75.47 and 57.24 MHz, respectively. Internal calibration of chemical shifts was performed relative to the chloroform peak for ^{1}H and $^{13}C\{^1H\}$ NMR spectra while external calibration was undertaken in the case of $^{77}Se\{^1H\}$ NMR spectra with respect to Ph_2Se_2 (δ 463 ppm relative to Me_2Se) in $CDCl_3$. A NitzschSTA 409 PC-Luxx TG-DTA instrument calibrated with $CaC_2O_4{\cdot}H_2O$ was used for thermogravimetric analyses (TGA). The TG curves were recorded at a heating rate of 10 °C min^{-1} under a flow of argon. A Philips PW-1820 diffractometer employing CuK_α radiation was utilised to record powder X-ray diffraction patterns. A 532 nm wavelength from a DPSS laser (OXXIUS-LC-532) was utilised to record the Raman spectra. The Raman-scattered light was detected using a CCD (ANDOR)-based monochromator (ANDOR-SR-750C) together with an edge filter. The FE-SEM and EDS measurements were

carried out on Zeiss Auriga and Oxford instruments, respectively. A Zeiss Libra 200 FE transmission electron microscope (TEM) operating at an accelerating voltage of 200 kV was used for TEM studies. The samples for TEM were prepared by placing a drop of sample dispersed in chloroform on a carbon-coated copper grid. Optical diffuse reflectance measurements in the range 200–1800 nm (0.68 eV to 6.2 eV) were performed on a JASCO V-670 two-beam spectrometer with a diffuse reflectance (DR) attachment consisting of an integration sphere coated with barium sulfate, which was used as a reference material. Measured reflectance data were converted to absorption (A) using the Kubelka–Munk remission function.[40] The band gaps of the samples were estimated by extrapolating the linear portion of the plot to the X (energy) axis.

X-ray crystallography

The crystallographic data for the complex $[Me_2Sn(SeC_4H_3N_2)_2]$ (**1**) were collected using CuK_α radiation (λ = 1.54184 Å) from a single crystal at 298(2) K on an XtaLAB Synergy, Dualflex, HyPix four-circle diffractometer with a micro-focus sealed X-ray tube using a mirror as a monochromator and a HyPix detector. All data were integrated with CrysAlis PRO, and a multi-scan absorption correction using SCALE3 ABSPACK was applied.[41] The structures were solved by iterative methods using OLEX and refined by full-matrix least-squares methods against F^2 by SHELXL-2017/1.[42,43] Hydrogen atoms were placed in idealised positions and were set riding on the respective parent atoms. All non-hydrogen atoms were refined with anisotropic thermal parameters. The structure was refined (weighted least squares refinement on F^2) to convergence. The crystal and structure refinement data are detailed in Table S1, SI. All figures were drawn using ORTEP and Mercury.[44,45] Crystallographic data (including structural factors) for the structures reported in this paper have been deposited with the Cambridge Crystallographic Data Centre (CCDC no. 2388509 for $[Me_2Sn(SeC_4H_3N_2)_2]$ (**1**)).

Electrochemical measurements

To analyse the performance of the supercapacitor, various electrochemical measurements, including cyclic voltammetry (CV), galvanostatic charge–discharge (GCD), and electrochemical impedance spectroscopy (EIS) were conducted using a three-electrode configuration. The CNT and CNT-TS films were utilised as the working electrode (WE). The electrochemical measurements were carried out using a CH1760E Bipot electrochemical workstation. In the case of three-electrode measurements, the reference electrode (RE) employed was Ag/AgCl (1 M saturated KCl), the counter electrode (CE) consisted of Pt wire, and 1 M KOH was used as the electrolyte. CV and GCD curves of the functionalized CNT substrate films are shown in Fig. S1.

Preparation of complex

Synthesis of $[Me_2Sn(2\text{-}SeC_4H_3N_2)_2]$ (1). To freshly prepared $NaSeC_4H_3N_2$—obtained by the reduction of $(SeC_4H_3N_2)_2$ (500 mg, 1.58 mmol) in a benzene–methanol solution using methanolic $NaBH_4$ (120 mg, 3.16 mmol)—solid Me_2SnCl_2 (348 mg, 1.58 mmol) was added, and the reaction mixture was stirred at room temperature for 3 h. The solvents were evaporated under vacuum, and the crude product was washed with hexane to remove excess or unreacted ligand. Subsequently, the pure product was extracted with dichloromethane, and the filtrate was reduced under vacuum and then slowly evaporated to obtain light-orange crystals. $[Me_2Sn(SeC_4H_3N_2)_2]$ (**1**): yield: 550 mg, 74.7%, m.p. 215 °C (melts with decomposition). Anal. calcd for $C_{10}H_{12}N_4SnSe_2$: C, 25.84; H, 2.60; N, 12.05%. Found: C, 25.90; H, 2.80; N, 12.10%. ^{1}H NMR ($CDCl_3$) δ (ppm): 1.11 (s, Me_2Sn, 6H, ^2J(Sn–H) = 74.9 Hz); 8.11 (s, 1H); 8.28 (s, 1H); 8.69 (s, 1H). $^{13}C\{^1H\}$ NMR ($CDCl_3$) δ (ppm): 4.8 (Me) (Me_2Sn, $^1J(^{119}Sn–^{13}C)$ = 483.7 Hz), 139.5, 142.7, 148.4, 155.6. $^{77}Se\{^1H\}$ NMR ($CDCl_3$) δ (ppm): 180 (s, $^1J(^{119}Sn–^{77}Se)$ = 718 Hz).

Preparation of nanostructures and their composites

Synthesis of tin selenide (SnSe) nanosheets. SnSe nanosheets were synthesised by thermolysis of $[Me_2Sn(SeC_4H_3N_2)_2]$ (**1**) (200 mg, 0.27 mmol) in oleylamine (7.0 mL) at 250 °C for 10 min through the heat-up method. The resulting dark solution was rapidly cooled, and 4.0 mL of toluene was added at 98 °C, followed by the addition of methanol to precipitate nanosheets at room temperature. Centrifugation and washing with a methanol/toluene mixture 2 : 1 were performed to separate the SnSe nanosheets. The sample was designated TS-1 and characterised with different tools.

Synthesis of tin selenide nanocomposites through pyrolysis. The complex $[Me_2Sn(SeC_4H_3N_2)_2]$ (**1**) (200 mg, 0.27 mmol) and g-C_3N_4 (15 mg) were mixed thoroughly before the mixture was introduced into a quartz boat and heated in a furnace under argon flow at 400 °C for 1 h. After cooling under argon, the black residue was named TS-2 and was subsequently characterised as trigonal $SnSe_2$ nanostructures.

Synthesis of tin selenide nanocomposites through thermolysis. Co-thermolysis of $[Me_2Sn(SeC_4H_3N_2)_2]$ (**1**) (200 mg, 0.27 mmol) and g-C_3N_4 (15 mg) in OAm (7.0 mL) was conducted using the heat-up method at 250 °C for 10 min. The dark solution formed was rapidly cooled, and 4.0 mL of toluene was added at 98 °C. Subsequently, excess methanol was added to precipitate the nanocomposite at room temperature. Centrifugation and washing with methanol/toluene mixture 2 : 1 were performed to separate the tin selenide nanocomposite. The sample was named TS-3 and characterized using different tools. In another experiment, the above procedure was repeated with only a change in the amount of g-C_3N_4 (7 mg). The resulting sample was named TS-4 and characterised.

Synthesis of functionalised CNT-tin selenide or/and g-C_3N_4 (FCNT-TS) electrodes. The energy storage performance of tin selenide and its composite samples (TS-1 to TS-4) was examined by coating them on CNT films, which were used as electrodes.[46] In order to coat tin selenide samples on the CNT film, a slurry was prepared by dispersing 5 mg of the sample, with Nafion (Sigma-Aldrich, CAS no. 27470-4) as a binder (10 wt%) in N-methyl-2-pyrrolidone (NMP, Sigma-Aldrich) by

ultrasonication for 10 min. The slurry was then brush-coated onto CNT film (2 cm × 2 cm). The mass loading of the TS was maintained at 1 mg per 4 cm^2. The brush-coated electrodes were dried at 100 °C overnight in an oven.

Results and discussion

Chemical synthesis and characterisation

The reaction of a sodium salt of pyrazinylselenolate with dimethyltin dichloride in 2 : 1 stoichiometry afforded pyrazinylselenolate complex, $[Me_2Sn(SeC_4H_3N_2)_2]$ (**1**) (Scheme 1) as a light-orange solid, soluble in most organic solvents. This solid when recrystallised in chloroform offered rod-shaped crystals. The complex was probed by multinuclear NMR, supported by elemental analyses. The ^1H and $^{13}C\{^1H\}$ NMR spectra presented the anticipated peaks and their multiplicities. The pyrazine ring proton resonances of $[Me_2Sn(SeC_4H_3N_2)_2]$ (**1**) were moved upfield relative to the equivalent signals for the pristine ligand. The $^{77}Se\{^1H\}$ NMR spectrum of $[Me_2Sn(SeC_4H_3N_2)_2]$ (**1**) presented only one peak at 180 ppm, pointing to the presence of a single species in the solution (ligand $^{77}Se\{^1H\}$ = 443 ppm). The $^{77}Se\{^1H\}$ NMR spectrum of complex **1** exhibited a single resonance at 180 ppm flanked by tin satellites with $^1J(^{119}Sn–^{77}Se)$ = 718 Hz, indicating direct interaction of Sn and Se. The selenium resonance peak of the complex shows that it is shielded with respect to the selenium signal of the diselenide ligand.

The estimated value of $^2J(^{119}Sn–^1H)$ of complex **1** is 74.9 Hz, less than the value anticipated for dimethyltin complexes with coordination number 6, while the magnitude of $^1J(^{119}Sn–^{13}C)$ (~483.7 Hz) is somewhat larger than those documented for tetra-coordinated diorganotin(IV) complexes.[47] The ∠C–Sn–C estimated for $[Me_2Sn(SeC_4H_3N_2)_2]$ (**1**) using the equation below is 117.85°,[48] while the same value determined by sc-XRD analysis is 127.32(16)°, indicating that the structure of complex **1** existing in the solid state also remains intact in the solution.

$$|^1J(^{119}Sn–^{13}C)| = 10.7(\angle C–Sn–C) – 778$$

X-ray crystallography for structural determination

Recrystallisation of $[Me_2Sn(SeC_4H_3N_2)_2]$ (**1**) was achieved by slow evaporation of a solution of **1** in chloroform to yield rod-shaped pale-yellow crystals. The molecular structure of $[Me_2Sn(SeC_4H_3N_2)_2]$ (**1**) with atomic numbering scheme and its crystal packing are revealed in Fig. 1. Certain inter-atomic parameters (bond length and angles) are given in Tables S1 and S2. The complex grows in a monoclinic crystal system (space group $P2_1/C$), while the unit cell constitutes four molecules of complex **1** (Fig. 1). The central Sn atom of $[Me_2Sn(SeC_4H_3N_2)_2]$ (**1**) is located on a C_2 axis with a distorted trapezoidal bipyramidal geometry defined by two methyl groups, and two selenium and two nitrogen atoms from two 2-pyrazine selenolate ligands, considering Sn···N weak interactions. The configuration around tin is similar to organo-tin pyridyl selenolates, $[Me_2Sn(2\text{-}SeC_5H_4N)_2]$,[22] $[Me_2Sn\{2\text{-}SeC_5H_3(Me\text{-}5)N\}_2]$[24] and the analogous thiolato complex, $[Me_2Sn(SC_5H_2N)_2]$.[49]

The Sn–Se bond distance (2.6175(4) and 2.6090(4)) are in agreement with those reported for $[^tBu_2Sn\{SeC_4H(Me\text{-}4,6)_2N_2\}_2]$ (2.615(3) and 2.618(3) Å) and $[^tBu_2Sn\{SeC_4H(Me\text{-}$

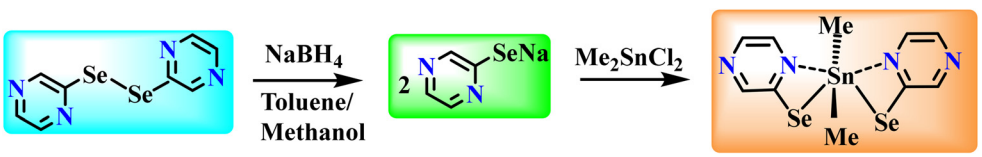

Scheme 1 Synthesis protocol for the preparation of $[Me_2Sn(SeC_4H_3N_2)_2]$ (**1**).

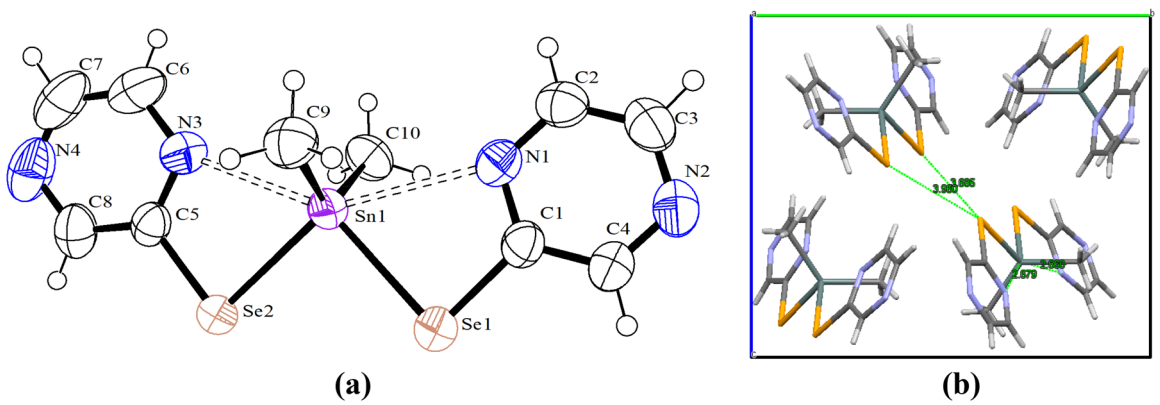

Fig. 1 (a) Molecular structure of monoclinic $[Me_2Sn(SeC_4H_3N_2)_2]$ (**1**) with the atomic number scheme (the ellipsoids are drawn with 50% probability) and (b) packing diagram of $[Me_2Sn(SeC_4H_3N_2)_2]$ (**1**) along the *a*-axis.

4,6)$_2$N$_2$}Cl] (2.583(3) and 2.595(3) Å)[23] and shorter than those reported for [Sn(SeC$_5$H$_4$N)$_2$]$_2$ (2.681, 2.759 Å)[17] [Sn(SePh)$_2$] (2.668, 2.675, 2.683, 2.673 Å)[50] and [^{t}Bu$_2$Sn(2-SeC$_5$H$_4$N)$_2$] (2.622(2) Å).[25,51] The molecule is slightly puckered with Sn⋯N distances (2.860 and 2.679 Å) longer than their covalent radii (2.15 Å), but are significantly smaller than the sum of their van der Waals (vdW) radii (3.72 Å),[52] suggesting a weak intramolecular interaction between tin and nitrogen atoms and in agreement with those reported for [Me$_2$Sn{2-SeC$_4$H(Me-4,6)$_2$N}$_2$] (2.671 Å).[28] These non-covalent interactions between Sn and tin present a case of chelation leading to a stable complex. The hexacoordination around tin is further corroborated by the ^1J(^{119}Sn–^{13}C) value of ~718 Hz, which falls in the range that is observed for six-coordination compounds of tin,[53] indicating that the weak interactions detected in the solid state are also present in solution. This is in contrast to what has been observed in [Me$_2$Sn{2-SeC$_5$H$_2$(Me-4,6)$_2$N}$_2$].[28] The Sn–C distances (2.118(4) and 2.126(3) Å) are in agreement with those of similar diorganotin pyridyl and pyrimidyl complexes[25–27,48] along with complexes of type [Me$_2$Sn(SC$_5$H$_4$N)$_2$] (~2.13 Å) and [Me$_2$Sn(C$_9$H$_6$NO)$_2$] (~2.15 Å).[48,54] The Se–Sn–Se bond angle in dimethyl tin complexes of pyridyl and pyrimidyl selenide are in the range of 91.23(4) to 94.25(8)°, while in the present case, the same angle falls at the lower end of the range, at 91.524(13)°.[22–25] The angles, ∠N–Sn–N and ∠Se–Sn–Se in **1** (145.10 and 91.57(2)°, respectively) are squeezed *vis-à-vis* the same angles in [Me$_2$Sn(SeC$_5$H$_4$N)$_2$] (152.1(2) and 94.25(8)°),[25] whereas ∠Se–Sn–Se is opened by ~4.5° relative to ∠S–Sn–S of bis[3-(2-pyridyl)-2-thienyl]di-*p*-tolylstannane (86.91(7)°).[55] Opening of ∠Se–Sn–Se with respect to ∠S–Sn–S might be expected because of the presence of a relatively more bulky Se atom in the former compared to the S atom in the latter. The N–Sn–Se bite angles (62.59° and 60.91°) of complex **1** are similar to those of the analogous dimethyltin complex with a 2-selenopyridyl ligand, [Me$_2$Sn(SeC$_5$H$_4$N)$_2$] (62.61° and 60.69°),[22] demonstrating that the ring effect has no impact on ∠N–Sn–Se bite angles.

The crystal packing of **1** in 3D space shows that the neighbouring [Me$_2$Sn(SeC$_4$H$_3$N$_2$)$_2$] (**1**) molecules are held together by short contacts between the Se2 atoms of two adjacent asymmetric units and the N2 atom of the asymmetric unit with the H atom of the C10B–H10B fragment of the nearby unit. The Se⋯Se distance (3.685 Å) is shorter than the vdW radius of the Se atoms (3.8 Å), suggesting weak secondary interactions. In contrast, the C10–H10B⋯N2 distances (C10–H10B⋯N2 = 2.693 Å) are shorter than the vdW radii of the two atoms (3.2 Å), signifying that strong non-bonding secondary interactions hold neighboring asymmetric units together. Additionally, adjoining asymmetric units in the same layer are sliding over each other through C–H⋯N interactions, while adjacent molecules in two bordering layers are linked together by weak Se⋯Se interactions.

Thermogravimetric analysis

Thermal traits of complex **1** were examined by thermogravimetric analysis (TGA) and differential thermogravimetry (DTG) (Fig. S2, SI) in the range of 30–1000 °C under a flowing argon atmosphere. The complex underwent a two-step decomposition. The first step had an onset temperature of 210 °C and a completion temperature of 300 °C with a weight loss of 83%. However, the experimental weight loss of 83% is significantly greater than the expected weight losses for SnSe (57.48%) and Sn (74.46%), pointing out the substantial volatility of the precursor, in turn making the precursor suitable for CVD applications.[56] The volatility of the precursor is corroborated by the presence of volatile pyrazine moieties in complex **1**. Additionally, a steady weight loss was noted even after 520 °C, which might be because of the loss of volatile tin.

Fabrication and characterisation of tin selenide nanostructures and their g-C_3N_4 composites

Gathering thermal behavioural inputs of complex **1** from the above measurements, a synthesis protocol for tin selenide (SnSe) nanosheets and their g-C_3N_4 composites has been planned by the thermolysis of [Me$_2$Sn(SeC$_4$H$_3$N$_2$)$_2$] (**1**) in the high-boiling coordinating solvent, oleylamine (OAm). A thermolysis temperature of 250 °C was preferred for the decomposition, even though the required decomposition temperature obtained from TG is 292 °C. This may be vindicated by the lowering of the thermal degradation temperature as a consequence of solvation of the complex by the coordinating solvent.[57] The selection of OAm as a solvent for thermolysis was driven by many factors: its high boiling point of 360 °C, the strong affinity of the nitrogen of the –NH$_2$ group for tin, leading to effective surface passivation of nanostructures and its role in catalysing of the thermal disintegration of the complex at relatively low temperatures compared to its solid-state decomposition temperature, as predicted by TG curves.[58] Thus, tin selenide nanosheets were synthesised by the heat-up method in OAm at 250 °C for 10 min. The p-XRD patterns (Fig. S3, SI) of the same exhibit Bragg's reflections at 2θ = 21.48, 25.35, 29.38, 30.62, 37.86, 41.38, 43.50, 44.30, 47.30, 49.70, 52.64, 54.21 and 57.50°, corresponding to orthorhombic SnSe (ICSD no. 12863; JCPDS no. 48-1224). These peaks can be marked as the reflections emanating from (101), (201), (011), (111), (311), (102), (202), (501), (112), (511), (312), (420) and (502), whereas peak broadening specifies that the particle dimensions are in the nano-region. In contrast, a tin selenide composite prepared through pyrolysis revealed reflections matching trigonal SnSe$_2$ (ICSD no. 43594; JCPDS no. 23-0602). While p-XRD patterns of g-C_3N_4 composites of tin selenide with different weight percentages of g-C_3N_4 prepared by thermolysis revealed peaks consistent with orthorhombic SnSe (ICSD no. 12863; JCPDS no. 48-1224) along with trigonal SnSe$_2$ (ICSD no. 43594; JCPDS no. 23-0602) (Fig. S4, SI). The extent of formation of SnSe$_2$ increases with the increasing amount of g-C_3N_4 used during the synthesis of the composites, which is determined by the relative intensities of SnSe and SnSe$_2$ peaks. The details of the reaction conditions and the phase of the material are listed in Table S3, SI.

Notably, the introduction of g-C_3N_4 to prepare an SnSe/g-C_3N_4 composite through a thermolysis experiment yields an

$SnSe$–$SnSe_2$/g-C_3N_4 composite instead of the required product, which has been designated as a tin selenide composite. This indicates that the addition of g-C_3N_4 drives the formation of $SnSe_2$ phase during the preparation of the composite. Furthermore, an attempt to prepare an $SnSe$/g-C_3N_4 composite by the pyrolysis of $[Me_2Sn(SeC_4H_3N_2)_2]$ (**1**) and g-C_3N_4 together in a furnace yields the $SnSe_2$/g-C_3N_4 composite (TS-2). The phase purity of these nanostructures and composites is further validated by their elemental compositions according to EDS (Fig. S5–S11, SI). These compositional studies revealed that the atom% ratio of Sn : Se is 1.01 : 1.00 and 1 : 1.92 for TS-1 and TS-2, respectively, confirming the SnSe and $SnSe_2$ compositions for these samples. Moreover, the uniform distribution of the integral elements within these samples was verified by 2D elemental mapping analysis.

The phase purity of rectangular SnSe nanosheets (TS-1) and hexagonal $SnSe_2$ (TS-2) was further evaluated by Raman spectroscopy in order to examine the binary-phase impurities present in the samples through the phonon modes of the nanomaterial. Further, the presence of g-C_3N_4 in composite samples can also be confirmed by Raman spectroscopy. The Raman spectrum of the TS-1 sample (Fig. S12, SI) exhibits a peak at 106 cm^{-1} and a shoulder at 156 cm^{-1} corresponding to the B_g and A_g modes of SnSe, while TS-2 shows peaks at 111 and 185 cm^{-1} related to in-plane E_g and out-of-plane A_{1g} modes of $SnSe_2$, consistent with literature reports for SnSe[59] and $SnSe_2$.[60]

The morphology, dimension and phase of TS-1 to TS-4 were determined by FE-SEM, TEM and selective area electron diffraction (SAED) patterns. SEM images of TS-1 and TS-2 revealed rectangular sheets and hexagonal sheets, as shown in Fig. 2(a) and (b), while SEM images of TS-3 and TS-4 revealed a mixture of rectangular and hexagonal sheets (Fig. 2(c) and (d)). TEM images of TS-1 to TS-4 (Fig. 2(e–h)) confirm the same. The average thickness of rectangular sheets (TS-1) and hexagonal sheets (TS-2) is 46 and 65 nm, respectively (Table S3, SI), while the lateral dimensions of the hexagonal sheets are in the range of 350–450 nm. SAED patterns of rectangular and hexagonal sheets exhibit lattice planes, (111), (511), (502) (Fig. 2(i)) and (002), (101), (103) (Fig. 2(j)), matching orthorhombic SnSe (ICSD no. 12863/JCPDS no. 48-1224) and trigonal $SnSe_2$ (ICSD no. 43594; JCPDS no. 23-0602) phases, respectively.

In contrast, the SAED patterns of TS-3 (Fig. 2(k)) and TS-4 (Fig. 2(l)) reveal the lattice planes (111) (SnSe), (011), (102), (003) ($SnSe_2$) and (201), (502) (SnSe), (002), (400), (110), (013) ($SnSe_2$), respectively, corresponding to orthorhombic SnSe and trigonal $SnSe_2$ indicating that both TS-3 and TS-4 contain a mixture of SnSe and $SnSe_2$, in conformity with the respective

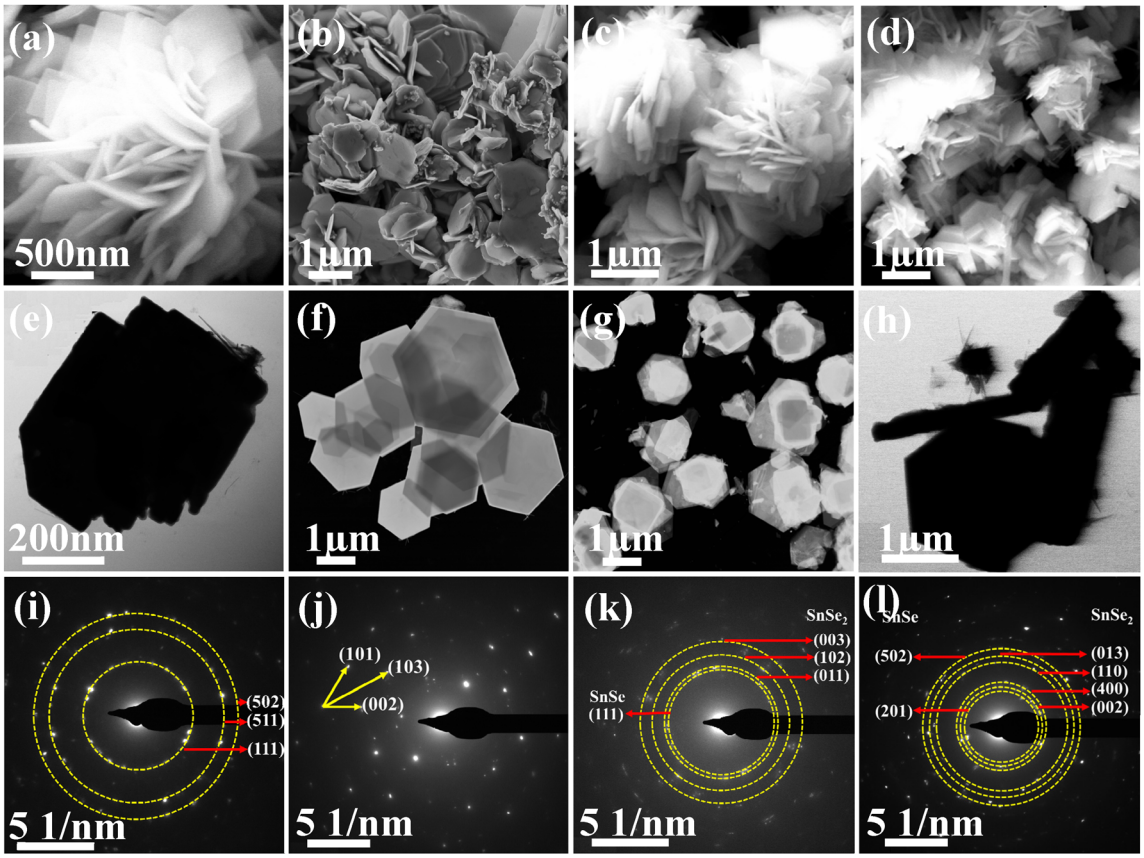

Fig. 2 (a–d) SEM images, (e–h) TEM images and (i–l) SAED patterns of rectangular SnSe nanosheets (TS-1), hexagonal $SnSe_2$ nanosheets/g-C_3N_4 composite (TS-2) and tin selenide/g-C_3N_4 nanocomposites (TS-3 and TS-4).

SEM and TEM images. The discrepancy between p-XRD and TEM sizes is mainly due to the dependency of the full width at half maximum of the p-XRD peak (which can be used to estimate particle size using the Scherrer equation) on crystal distortions, defects and instrumental broadening in addition to scattering domain size.[61]

Exploring the optical behaviour of tin selenide nanosheets and g-C_3N_4 nanocomposites

SnSe and $SnSe_2$ have direct-band gaps of 1.3 (ref. 41) and 1.84 eV,[62] respectively, with an absorption coefficient of $\sim 10^5$ cm^{-2}, a high carrier concentration and p-type conductivity, and they show significant applicability in solar photovoltaics,[63] thermoelectrics[64] photodetectors, anode materials for batteries[65] and supercapacitors.[66] Besides, the effectiveness of these applications can be further boosted by replacing the bulk materials with their nanostructures, due to dimension-driven and morphology-driven changes in properties. Of these properties, the optical band gap is worth investigating as it has an impact on the efficiency of these applications. Hence, probing of the optical bandgap of the synthesised nanosheets and composites by diffused reflectance spectroscopy (DRS) is worthwhile. These band gap measurements were carried out by plotting $[F(R)]^n$ *vs.* energy ($h\nu$), where $F(R)$ is the Kubelka–Munk (KM) function, which can be stated as follows:

$$[F(R)]^n = A(h\nu - E_g)$$

where $h\nu$, A, E_g are photon energy, a constant, and the band gap when $n = \frac{1}{2}$ or 2 for indirect- or direct-band gaps. The direct-band gap values of these nanosheets and nanocomposites were estimated using the aforementioned plots where $n = 2$ (Fig. 3). The direct-band gap values of rectangular SnSe (TS-1), hexagonal $SnSe_2$-nanosheets (TS-2), and tin selenide/g-C_3N_4 composites (TS-3 and TS-4) of 1.85, 2.21, 1.89 and 1.91 eV (Table S3, SI) were blue shifted relative to the bulk values (direct-band gap values for bulk SnSe and $SnSe_2$ are 1.3 (ref. 9) and 1.84 eV,[62] respectively), which may be due to various factors, such as quantum confinement, lattice distortion or surface lattice defects.

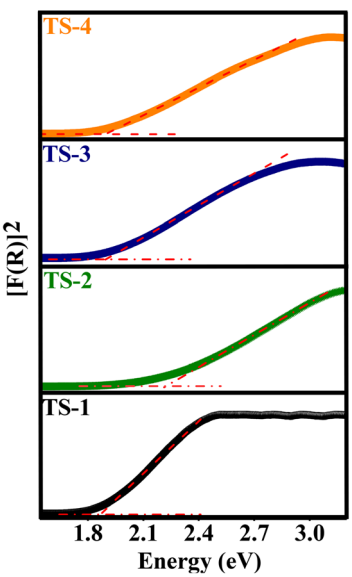

Fig. 3 Plots of $[F(R)]^2$ *vs.* energy (eV) created by KM transformation of DRS data of TS-1 to TS-4, for calculating direct-band gap energies.

As Bohr's radius of bulk SnSe is around 23 nm (ref. 67) and the thickness of rectangular sheets (TS-1) and hexagonal sheets (TS-2) in the present study is 46 and 65 nm, respectively, quantum confinement may be ruled out. Hence, the blue shift in band gap values can be ascribed either to lattice distortion or to surface lattice defects. Nevertheless, band gap values of all the samples (TS-1 to TS-4) are in the range 1.85–2.21 eV, indicating their reasonable conductivity and suitability as materials for supercapacitors.

Electrochemical performance of tin selenide nanosheets and composite nanostructures

The pristine SnSe rectangular nanosheets (TS-1) and tin selenide/g-C_3N_4 composites (TS-2, TS-3 and TS-4) with band gaps in the range of 1.85–2.21 eV are appropriate for a supercapacitor. Given this, these samples were evaluated for supercapacitor applications, and cyclic voltammetry (CV), electrochemical impedance spectrometry (EIS), galvanostatic charge–discharge (GCD), and cyclic stability studies were performed in a three-electrode setup employing a 1 M KOH solution as the electrolyte to investigate the supercapacitor performance.

To develop flexible supercapacitors, all solid-state supercapacitors (SSCs) were employed using SnSe nanosheets (TS-1) and their g-C_3N_4 composites (TS-2, TS-3 and TS-4) as active materials. The energy storage performance of these samples was studied by coating the samples on CNT film, as reported elsewhere[46] and using these coated CNT films as electrodes. Fig. 4(a) and (b) depict CV analytical results performed on TS-1 to TS-4 electrodes. The CV plots of CNT-TS (Fig. 4(a)) were acquired at a scan rate of 100 mV s^{-1} and a potential range of −0.6 to 0.4 V. The CV plots are symmetric and nearly rectangular due to the surface electro-sorption and the subsequent reversible surface redox reactions of SnSe nanosheets (TS-1) using cations/anions.

The larger surface area under the CV curve of TS-3, relative to the other electrodes, specifies a higher capacitance for the TS-3 electrode. GCD measurements were performed to evaluate the specific capacitance of the flexible electrodes. Fig. 4(b) reveals the GCD shapes of the TS-1 to TS-4 electrodes. All TS electrodes display a non-linear GCD profile, representing the pseudocapacitive nature of faradaic reactions in the TS. The TS-3 electrode shows an extended charge–discharge time, signifying its higher capacitance relative to the other electrodes. This improvement can be attributed to the synergistic effect between SnSe nanosheets and g-C_3N_4. The incorporation of g-C_3N_4 enhances the electrochemical pseudocapacitance by providing additional redox-active sites, increasing surface area, and facilitating better ion diffusion throughout the electrode matrix. The specific capacitance (C_s) is determined with the following formula:

$$C_s = (I \times \Delta t)/(m \times \Delta V)$$

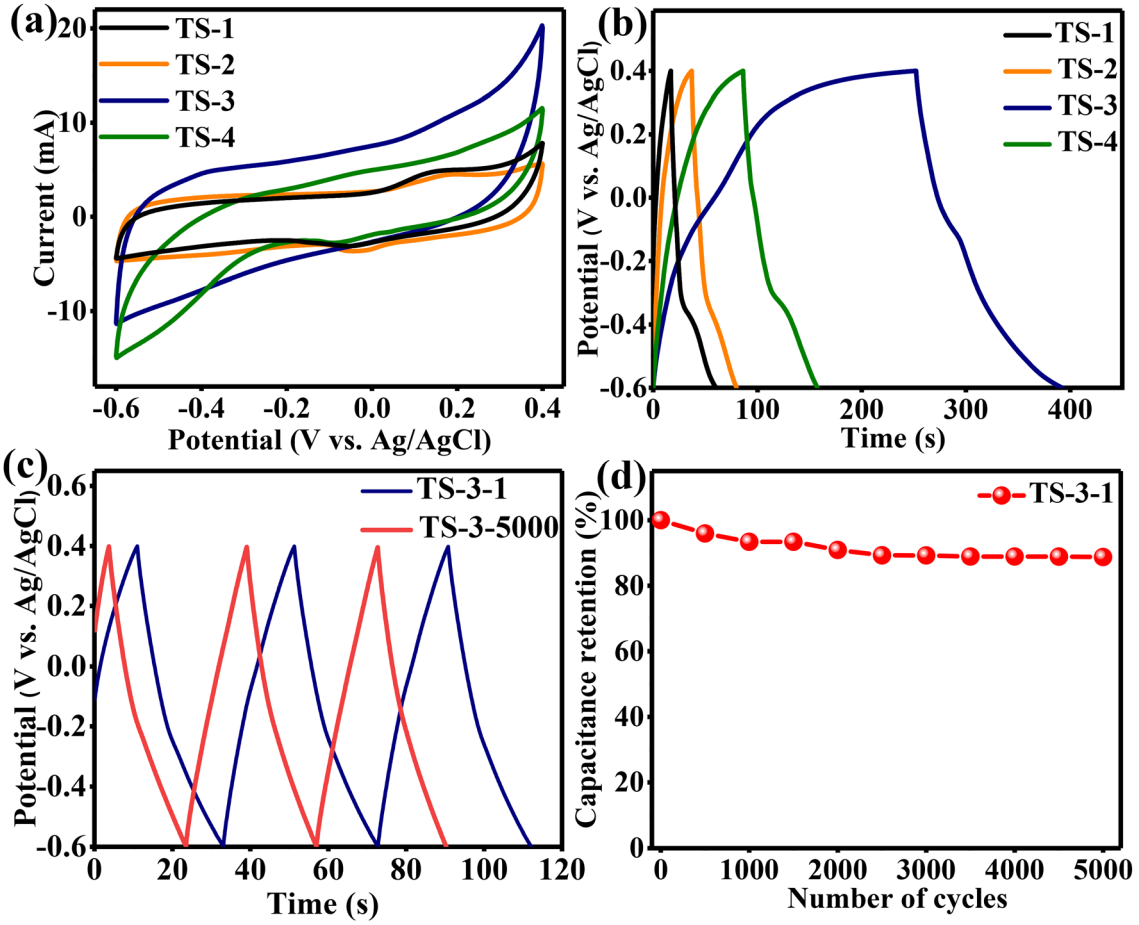

Fig. 4 (a) CV at 100 mV s^{-1} in 1 M KOH and (b) GCD analyses of electrodes made up of TS-1 to TS-4 in the three-electrode configuration at 1 A g^{-1}, while (c) and (d) represent 1st and 5000th GCD plots at 3 A g^{-1} and cyclic stability of TS-3 electrode demonstrating 85% capacitance retention after 5000 cycles of charge–discharge.

where I, Δt, m and ΔV denote the discharge current, discharge time, active material loading and the voltage window, respectively. The TS-3 electrode unveils a specific capacitance of 140 F g^{-1} at 1 A g^{-1}, which is meaningfully higher than the specific capacitance of the other electrodes (Table S4, SI). The prolonged cyclic steadiness of the TS-3 electrodes was examined *via* charge–discharge cycles at 3 A g^{-1}. Fig. 4(c) and (d) confirm the outstanding cyclic durability of the TS-3 electrode, retaining 85% capacitance even after 5000 cycles. Fig. 5 shows the electrochemical impedance spectra (EIS) of the TS-1 to TS-4 electrodes, where TS-3 demonstrates a quasi-vertical profile with an equivalent series resistance of ~3 Ω. The electrochemical impedance spectra (EIS) of the TS-1 to TS-4 electrodes exhibit a quasi-vertical line in the low-frequency region, indicative of ideal capacitive behavior and efficient ion diffusion. The Nyquist plot also shows a small semicircle in the high-frequency region, corresponding to the charge transfer resistance (R_{ct}), and a low equivalent series resistance (ESR) of ~3 Ω, suggesting low internal resistance. The TS-3 electrode shows the lowest R_{ct}, which can be attributed to the synergistic interaction between SnSe nanosheets and g-C_3N_4, which enhances the electrode–electrolyte interface, reduces charge transfer resistance, and facilitates faster ion transport. This behavior is consistent with its superior electrochemical performance observed in CV and GCD measurements.

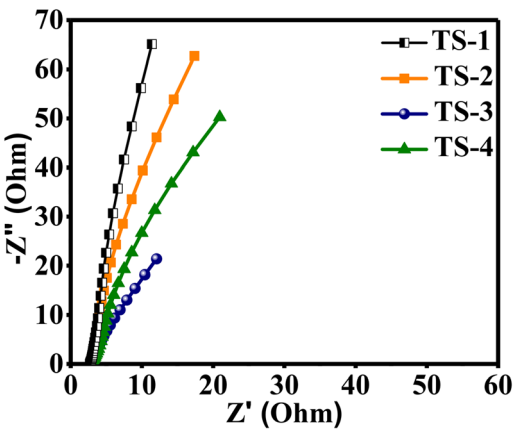

Fig. 5 Electrochemical impedance spectra (EIS) of TS-1 to TS-4 electrodes.

Conclusions

It is notable that the synthesis of phase-pure tin selenides employing dual sources consistently involves subtle nuances. Therefore, the molecular template method for the synthesis of quality tin selenide nanostructures is simple and accessible. Consequently, a new, air-stable and moisture-stable pyrizinylselenolate of tin(IV), $[Me_2Sn(SeC_4H_3N_2)_2]$, has been produced, structurally characterized and used as a molecular template for the synthesis of SnSe nanosheets and tin selenide/g-C_3N_4 composites. These materials were evaluated for their crystal structure, shape, and energy gap. Experimentally determined optical energy gaps of these materials are in a suitable range for a supercapacitor material. A supercapacitor made up of a tin selenide/g-C_3N_4 composite (TS-3) remained stable for more than 5000 cycles and established a specific capacitance of 140 F g^{-1} at a current density of 1 A g^{-1}, showing good cyclability with reasonable specific capacitance. Even though the molecular template method is quite versatile for metal chalcogenides, the applicability of these materials for supercapacitors is still to be determined. Hence, the current study of the molecular templated synthesis of tin selenide and its composites for supercapacitor applications can overcome the application blockade.

Author contributions

N. K., D. N., and J. P. were responsible for data curation, formal analysis, investigation, validation, visualisation, and writing – original draft. S. S. P. was responsible for conceptualisation, data curation, formal analysis, investigation, validation, resources, and writing – review & editing. S. C. contributed to data curation, formal analysis and investigation. A. W. and S. K. contributed to data curation, investigation, and validation. G. K. was responsible for conceptualisation, formal analysis, investigation, methodology, project administration, resources, supervision, validation, writing – original draft and writing – review & editing.

Conflicts of interest

The authors declare no conflicts of interest.

Data availability

EDS spectra and 2D mapping of the constituent elements of TS-1 to TS-4. See DOI: **https://doi.org/10.1039/d5dt01255d**.

CCDC 2388509 contains the supplementary crystallographic data for this paper.[68]

Acknowledgements

We would like to express our gratitude to Dr A. C. Bhasikuttan, Associate Director of the Chemistry Group and Dr N. Choudhury, Chemistry Division at Bhabha Atomic Research Centre, for their support of this work. We also extend our thanks to the Head of the Radiation Technology Development Division (RTDD) for their assistance with the TG measurements. S. S. P. gratefully acknowledges Prof. David Portehault, Laboratoire de Chimie de la Matière Condensée de Paris (LCMCP), Sorbonne Université, for his kind support.

References

1 W. Shi, M. Gao, J. Wei, J. Gao, C. Fan, E. Ashalley, H. Li and Z. Wang, *Adv. Sci.*, 2018, **5**, 1700602–1700624.
2 M. Kang, S. Rathi, I. Lee, L. Li, M. A. Khan, D. Lim, Y. Lee, J. Park, A. T. Pham, A. T. Duong, S. Cho, S. J. Yun and G. H. Kim, *J. Nanosci. Nanotechnol.*, 2017, **18**, 4243–4247.
3 Z. Li, Y. Guo, F. Zhao, C. Nie, H. Li, J. Shi, X. Liu, J. Jiang and S. Zuo, *RSC Adv.*, 2020, **10**, 16749–16755.
4 X. Wang, Y. Liu, J. Dai, Q. Chen, X. Huang and W. Huang, *Chem. – Eur. J.*, 2020, **26**, 3870–3876.
5 Y. Sun, Z. Zhong, T. Shirakawa, C. Franchini, D. Li, Y. Li, S. Yunoki and X. Q. Chen, *Phys. Rev. B: Condens. Matter Mater. Phys.*, 2013, **88**, 235122.
6 Z. Li, J. Ding and D. Mitlin, *Acc. Chem. Res.*, 2015, **48**, 1657–1665.
7 S. S. Pathak, S. Dey, A. Kumar, S. Gamre, T. Gadly and G. Kedarnath, *J. Phys. Chem. C*, 2024, **128**(19), 8058–8067.
8 Y. Tomar, S. S. Pathak, S. Jain and L. S. Panchakarla, *Isr. J. Chem.*, 2022, **62**, e202100080.
9 J. M. Gonzalez and I. I. Oleynik, *Phys. Rev. B*, 2016, **94**, 125443.
10 C. Chang, M. Wu, D. He, Y. Pei, C. F. Wu, X. Wu, H. Yu, F. Zhu, K. Wang, Y. Chen, L. Huang, J. F. Li, J. He and L. D. Zhao, *Science*, 2018, **360**, 778–783.
11 L. D. Zhao, S. H. Lo, Y. S. Zhang, H. Sun, G. J. Tan, C. Uher, C. Wolverton, V. P. Dravid and M. G. Kanatzidis, *Nature*, 2014, **508**, 373–377.
12 Z. Shao, Z. G. Fu, S. Li, Y. Cao, Q. Bian, H. Sun, Z. Zhang, H. Gedeon, X. Zhang, L. Liu, Z. Cheng, F. Zheng, P. Zhang and M. Pan, *Nano Lett.*, 2019, **19**, 5304–5312.
13 Z. Wei, L. Wang, M. Zhuo, W. Ni, H. Wang and J. Ma, *J. Mater. Chem. A*, 2018, **6**, 12185–12214.
14 Y. Fan, J. Wang and M. Zhao, *Nanoscale*, 2019, **11**, 14836–14843.
15 M. Wang, Z. Wang, X. Xu, S. Duan and C. Du, *Nanotechnology*, 2019, **30**, 265703.
16 D. Ni, Y. Chen, X. Yang, C. Liu and K. Cai, *J. Alloys Compd.*, 2018, **737**, 623–629.
17 F. Hartl, V. Brune, S. Lüggert, C. Hegemann, D. van Gerven, M. Wilhelm, S. Ji, H. Choi and S. Mathur, *Inorg. Chem.*, 2023, **62**, 6274–6287.
18 S. Wu, S. Zhou, Q. Feng, H. Zhao, X. Xu, T. Cui, H. Zhang, X. Wang and Q. Yang, *J. Energy Storage*, 2021, **42**, 103032.
19 B. Pandit, C. D. Jadhav, P. G. Chavan, H. S. Tarkas, J. V. Sali, R. B. Gupta and B. R. Sankapal, *IEEE Trans. Power Electron.*, 2020, **35**, 11344–11351.

20 P. Boudjouk, D. J. Seidler, D. Grier and G. J. McCarthy, *Chem. Mater.*, 1996, **8**, 1189–1196.
21 Y. Cheng, T. J. Emge and J. G. Brennan, *Inorg. Chem.*, 1996, **35**, 342–346.
22 I. Y. Ahmet, J. R. Thompson and A. L. Johnson, *Eur. J. Inorg. Chem.*, 2018, 1670–1678.
23 J. R. Thompson, I. Y. Ahmet, A. L. Johnson and G. Kociok-Köhn, *Eur. J. Inorg. Chem.*, 2016, 4711–4720.
24 S. R. Bahr, P. Boudjouk and G. J. McCarthy, *Chem. Mater.*, 1992, **4**, 383–388.
25 R. K. Sharma, G. Kedarnath, A. Wadawale, C. A. Betty, B. Vishwanadh and V. K. Jain, *Dalton Trans.*, 2012, **41**, 12129–12138.
26 A. Tyagi, G. Kedarnath, A. Wadawale, A. Y. Shah, V. K. Jain and B. Vishwandh, *RSC Adv.*, 2016, **6**, 8367–8376.
27 A. Tyagi, G. Karmakar, A. Wadawale, A. Y. Shah, G. Kedarnath, A. P. Srivastava, V. Singh and V. K. Jain, *J. Organomet. Chem.*, 2018, **873**, 15–21.
28 G. Karmakar, K. K. Halankar, A. Tyagi, B. P. Mandal, A. P. Wadawale, G. Kedarnath, A. P. Srivastava and V. Singh, *Dalton Trans.*, 2021, **50**, 15730–15742.
29 P. Kevin, S. N. Malik, M. A. Malik and P. O'Brien, *Chem. Commun.*, 2014, **50**, 14328–14330.
30 M. D. Khan, M. Aamir, M. Sohail, M. Sher, N. Baig, J. Akhtar, M. A. Malik and N. Revaprasadu, *Dalton Trans.*, 2018, **47**, 5465–5473.
31 C. Gurnani, S. L. Hawken, A. L. Hector, R. Huang, M. Jura, W. Levason, J. Perkins, G. Reid and G. B. G. Stenning, *Dalton Trans.*, 2018, **47**, 2628–2637.
32 C. H. de Groot, C. Gurnani, A. L. Hector, R. Huang, M. Jura, W. Levason and G. Reid, *Chem. Mater.*, 2012, **24**, 4442–4449.
33 M. A. Dar, S. R. Ahmed, M. A. Rather, S. Kalpana, A. A. Rather, S. R. Ahamed and Z. Ahmad, *Inorg. Chem. Commun.*, 2023, **153**, 110838.
34 C. Zhang, H. Yin, M. Han, Z. Dai, H. Pang, Y. Zheng, Y. Q. Lan, J. Bao and J. Zhu, *ACS Nano*, 2014, **8**, 3761–3770.
35 G. Kedarnath, in *Handbook on synthesis strategies for advanced materials*, ed. A. K. Tyagi and R. S. Ningthoujam, Springer Singapore, Singapore, 2021, vol. 15, pp. 467–501.
36 G. Kedarnath and V. K. Jain, *New J. Chem.*, 2023, **47**, 20688.
37 N. Kushwah, S. Chopade, A. Wadawale, P. B. Sharma and G. Kedarnath, *RSC Adv.*, 2023, **13**, 36392.
38 A. Kaushal, R. Alexander, D. Mandal, J. B. Joshi and K. Dasgupta, *Chem. Eng. J.*, 2023, **452**, 139142.
39 R. Alexander, A. Kaushal, J. Prakash, P. T. Rao, D. Sen and K. Dasgupta, *J. Porous Mater.*, 2023, **30**, 507–520.
40 B. Philips-Invernizzi, D. Dupont and C. Cazé, *Opt. Eng.*, 2001, **40**, 1082–1092.
41 P. D. Antunez, J. J. Buckley and R. L. Brutchey, *Nanoscale*, 2011, **3**, 2399–2411.
42 *Rigaku Oxford Diffraction, CrysAlis PRO*, Rigaku Oxford Diffraction, Yarnton, England, 2015.
43 O. V. Dolomanov, L. J. Bourhis, R. J. Gildea, J. A. K. Howard and H. Puschmann, *J. Appl. Crystallogr.*, 2009, **42**(2), 229–341.
44 G. M. Sheldrick, *Acta Crystallogr., Sect. C*, 2015, **71**, 3–8.
45 (*a*) L. J. Farrugia, *J. Appl. Crystallogr.*, 1997, **30**, 565; (*b*) C. F. Macrae, P. R. Edgington, P. McCabe, E. Pidcock, G. P. Shields, R. Taylor, M. Towler and J. van der Streek, *J. Appl. Crystallogr.*, 2006, **39**, 453–457.
46 D. Nechiyil, J. Mor, R. Alexander, S. K. Sharma, K. Dasgupta and J. Prakash, *J. Energy Storage*, 2024, **85**, 111207.
47 C. Vatsa, Ph. D. Thesis, University of Mumbai, 1990.
48 T. P. Lockhart and F. Davidson, *Organometallics*, 1987, **6**, 2471–2478.
49 M. V. Castaño, A. Macías, A. Castiñeiras, A. S. González, E. G. Martínez, J. S. Casas, J. Sordo, W. Hiller and E. E. Castellano, *J. Chem. Soc., Dalton Trans.*, 1990, 1001–1005.
50 A. Eichhöfer, J. J. Jiang, H. Sommer, F. Weigend, O. Fuhr, D. Fenske, C. Y. Su and G. Buth, *Eur. J. Inorg. Chem.*, 2010, 410–418.
51 J. Otera, T. Yano and K. Kusakabe, *Bull. Chem. Soc. Jpn.*, 1983, **56**, 1057–1059.
52 A. Bondi, *J. Phys. Chem.*, 1964, **68**, 441–452.
53 T. P. Lockhart, W. F. Manders and J. J. Zuckerman, *J. Am. Chem. Soc.*, 1985, **107**, 4546–4547.
54 E. O. Schlemper, *Inorg. Chem.*, 1967, **6**, 2012–2017.
55 P. J. Smith and A. P. Tupciauskas, *Annu. Rep. NMR Spectrosc.*, 1978, **8**, 291–370.
56 J. R. Thompson, I. Y. Ahmet, A. L. Johnson and G. Kociok-Köhn, *Eur. J. Inorg. Chem.*, 2016, 4711–4720.
57 N. Kushwah, G. Kedarnath, A. Wadawale, K. K. Halankar, B. P. Mandal, M. Jafar and B. Vishwanadh, *Inorg. Chem.*, 2024, **62**, 8823–8834.
58 M. D. Khan, M. Akhtar, M. A. Malik, N. Revaprasadu and P. O'Brien, *ChemistrySelect*, 2018, **3**, 2943–2950.
59 X. Z. Li, J. Xia, L. Wang, Y. Y. Gu, H. Q. Cheng and X. M. Meng, *Nanoscale*, 2017, **9**, 14558.
60 H. Guan, H. Li, J. Ming, J. Hong, J. Dong, W. Qiu, W. Zhu, J. Yu, Z. Chen, G. Peng and H. Lu, *J. Lightwave Technol.*, 2020, **38**, 6089–6096.
61 (*a*) L. J. Farrugia, *J. Appl. Crystallogr.*, 1997, **30**, 565; (*b*) C. F. Macrae, P. Edgington, P. McCabe, E. Pidcock, G. P. Shields, R. Taylor, M. Towler and J. van der Streek, *J. Appl. Crystallogr.*, 2006, **39**, 453–457.
62 M. Kumar, S. Rani, Y. Singh, K. S. Gour and V. N. Singh, *RSC Adv.*, 2021, **11**, 6477–6503.
63 M. Kumar, S. Rani, Y. Singh, Mamta, A. Kumar and V. N. Singh, *Sol. Energy*, 2022, **232**, 146–153.
64 M. W. van de Putte and M. Huijben, *Appl. Surf. Sci.*, 2023, **623**, 157034.
65 Z. Wei, L. Wanga, M. Zhuo, W. Ni, H. Wang and J. Ma, *Mater. Chem. A*, 2018, **6**, 12185–12214.
66 S. Harish and P. U. Sathyakam, *J. Energy Storage*, 2022, **52**, 104966.
67 J. J. Buckley, F. A. Rabuffetti, H. L. Hinton and R. L. Brutchey, *Chem. Mater.*, 2012, **24**, 3514–3516.
68 N. Kushwah, D. Nechiyil, J. Prakash, S. M. Chopade, S. S. Pathak, A. Wadawale, S. Kumar and G. Kedarnath, CCDC 2388509: Experimental Crystal Structure Determination, 2025, DOI: **10.5517/ccdc.csd.cc2l5fpx**.